



## ORIGINAL ARTICLE OPEN ACCESS

# Dissection of Behavioral Components and the Role of Omega/Delta Turns for the Chemotaxis of *C. elegans*

Karin Suwazono  | Koyo Kuze | Ukyo T. Tazawa  | Moon Sun Jang  | Hirofumi Kunitomo  | Yu Toyoshima  | Yuichi Iino 

Department of Biological Sciences, Graduate School of Science, The University of Tokyo, Tokyo, Japan

**Correspondence:** Yuichi Iino ([iino@bs.s.u-tokyo.ac.jp](mailto:iino@bs.s.u-tokyo.ac.jp))

**Received:** 19 March 2025 | **Revised:** 8 May 2025 | **Accepted:** 9 May 2025

**Transmitting Editor:** Noriko Osumi

**Funding:** This work was supported by the Japan Science and Technology Agency (JPMJCR22N4) and the Japan Society for the Promotion of Science (22H00416, 23K18149).

## ABSTRACT

The chemotactic mechanism of the nematode *Caenorhabditis elegans* primarily consists of two components: the pirouette mechanism and the weathervane mechanism. The pirouette mechanism is a form of klinokinesis that regulates the frequency of rapid reorientation behaviors called pirouettes, which include omega/delta turns, while the weathervane mechanism involves gradual directional adjustments. Furthermore, previous studies have shown that in pirouettes, not only is the frequency of reorientation regulated, but the reorientation angle is also adjusted. However, conventional centroid-based analyses have left the postural dynamics during turns unresolved. In this study, we tracked the movement of individual worms during chemotaxis and determined the centerlines representing worm postures. From these data, we extracted turning behaviors, classified postural patterns, and quantified directional changes during turns. Our results indicate that the reorientation angle is modulated during turns to orient the animal toward the desired chemical concentrations. Additionally, we found the diversity of postural dynamics and directional changes in turn sequences. A detailed classification of turn sequences revealed that directional turning is achieved by selection of specific sequence types and adjustment of turning angles. This study provides the most detailed and quantitative analysis to date of the turning behaviors as a fundamental component of *C. elegans* chemotaxis.

## 1 | Introduction

All motile animals are endowed with motor programs that support survival and species propagation, such as finding food, escaping from predators, seeking mating partners, and engaging in courtship behaviors. Understanding the structure of the motor programs is therefore one of the main focuses of ethology and neuroscience. The nematode *Caenorhabditis elegans*, a widely utilized model organism in neuroscience and behavioral genetics, exhibits chemotaxis, where it moves toward high or low concentrations, or a specific concentration, of odorants or water-soluble chemicals. Unlike vision, which provides spatial

information over a visible range, chemosensation only provides local concentration cues at the sensory organ's contact points. As a result, *C. elegans* needs to detect changes in chemical concentration associated with its own movement and select appropriate behaviors to reach the desired concentration. To date, two primary mechanisms underlying *C. elegans* chemotaxis have been identified: the weathervane mechanism and the pirouette mechanism.

In the weathervane mechanism, the worm gradually curves toward a favorable direction while moving forward (Iino and Yoshida 2009) (Figure 1A, left). The weathervane mechanism

This is an open access article under the terms of the [Creative Commons Attribution-NonCommercial-NoDerivs](https://creativecommons.org/licenses/by-nc-nd/4.0/) License, which permits use and distribution in any medium, provided the original work is properly cited, the use is non-commercial and no modifications or adaptations are made.

© 2025 The Author(s). *Genes to Cells* published by Molecular Biology Society of Japan and John Wiley & Sons Australia, Ltd.

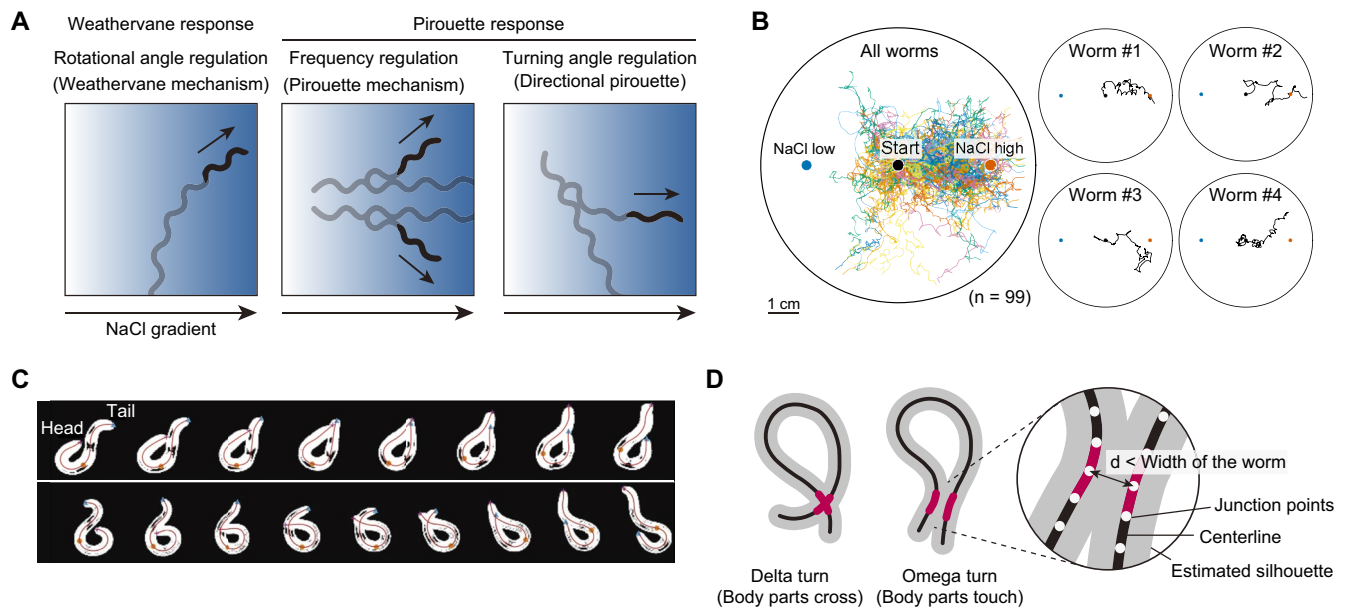


**FIGURE 1** | Definition of turns using centerline data. (A) Schematic drawing of chemotaxis strategies known in *C. elegans*. Blue graded color in the background represents NaCl concentration. (left) In the weathervane mechanism, as a form of klinotaxis, worms gradually curve toward higher NaCl concentration. (center) In pirouette mechanism, as a form of klinokinesis, the animals show increased rates of pirouette, a bout of reversal and sharp turns, when the NaCl concentration decreases upon their forward locomotion. (right) In pirouette responses, worms show directionality, so that the turning angle is not random as assumed in klinokinesis, but is biased toward higher NaCl concentration. (B) (left) Trajectory of all animals on the chemotaxis plate were overlaid. Different colors were used for each worm. (right) Example trajectory of four worms. These animals show chemotaxis to the NaCl-high peak on the plate with NaCl gradient. (C) Examples of centerline extraction from worm movies obtained. Fluorescence worm images were binarized (white), and the centerline (red) was determined from the binary images. (D) Types of turns and their identification based on centerlines. All cases where any two segments of the centerline (in red) were within the length of  $d = 7 \times$  segment length, the postures were judged as turns.

is a form of klinotaxis (Fraenkel and Gunn 1961; Bell and Tobin 1982), in which the animal samples stimulus intensity on both sides of its body axis to determine the behavioral response (Fraenkel and Gunn 1961). In contrast, in the pirouette mechanism, the frequency of pirouettes—a series of rapid reorientation movements occurring with short intervals—increases when the chemical concentration change is unfavorable (Pierce-Shimomura et al. 1999) (Figure 1A, center). Similar navigation strategies have been observed in the response to salts (Iino and Yoshida 2009; Pierce-Shimomura et al. 1999) and odorants (Albrecht and Bargmann 2011; Yamazoe-Umemoto et al. 2015), as well as to temperature (Ryu and Samuel 2002; Luo et al. 2014a; Ikeda et al. 2020). These observations suggest that *C. elegans* employs a set of flexible and common navigational strategies across different sensory modalities.

The pirouette mechanism was initially considered a form of klinokinesis, where the frequency of random reorientation is modulated based on the intensity of sensory inputs (Fraenkel and Gunn 1961; Bell and Tobin 1982; Tanimoto et al. 2017). However, as demonstrated in (Pierce-Shimomura et al. 1999; Jang et al. 2019), the pirouette response is regulated not only in frequency but also in directionality. Specifically, the reorientation angle during a pirouette is adjusted based on the chemical concentration gradient before the pirouette, a phenomenon known as directional pirouettes (Jang et al. 2019) (Figure 1A, right).

A pirouette was originally defined based on worm centroid tracking results as a bout of sharp directional changes of centroid

movement that occur with short intervals (Pierce-Shimomura et al. 1999); it includes complex movements such as alternating short bouts of backward movements and reorientation behaviors such as omega turns. To identify which elements of the pirouette response contribute to directionality, in (Jang et al. 2019), the centroid movement data of chemotaxing worms were analyzed. This analysis suggested that transitions between forward and backward movement, as well as omega turns, contribute to salt chemotaxis.

Omega turns are characterized by the head touching the ventral side of the body (Croll 1975); these turns frequently occur immediately after the transition from prolonged backward movement to forward movement (Gray et al. 2005; Zhao et al. 2003). Another form of turn, the delta turn, involves an even deeper body bend than the omega turn, with the head crossing over the body (Broekmans et al. 2016). Centroid-based analyses on time-lapse images of a population of animals as in (Jang et al. 2019) enabled precise tracking of simple locomotion of individual animals. However, turning behaviors were identified merely based on the roundness of the worm's body silhouette, making turn identification and quantification less accurate. As a result, the postural dynamics during turns remained unclear.

In this study, we conducted a detailed analysis of posture transitions during these turns using centerline data obtained from high-resolution images of individual chemotaxing worms. Our analyses revealed that the direction of turns are actively regulated depending on the chemical gradient. Furthermore, a

detailed classification of turns showed that directional turns result from the selection of specific sequence types and the adjustment of turning angles.

## 2 | Results

### 2.1 | Definition of Turns Using Centerline Data

A pirouette has been originally defined as consecutive sharp directional changes of worm centroid movement. It is usually initiated by a reversal, in which the worm switches from forward to backward locomotion, followed by various combinations of turning and reversals, and terminated by resumption of forward locomotion. Previous studies have shown that pirouettes are modulated not only in frequency but also in reorientation angles to drive salt chemotaxis (Pierce-Shimomura et al. 1999; Jang et al. 2019). Backward locomotion can be followed by turning behaviors such as omega and delta turns, where the head contacts or crosses the body, or other deep bends where the head does not contact the body. The previous study further suggested that turning angles of omega/delta turns within pirouettes are by themselves regulated to improve the worm orientation (Jang et al. 2019). However, these studies analyzed only centroid movement, leaving it unclear how animals behave to attain the proper direction.

To address how turning behaviors are regulated depending on chemical gradient, we individually tracked and recorded 99 animals navigating NaCl gradients (Figure 1B) and extracted time-series centerline data from video recordings (Figure 1C) for detailed analysis of turns. Because *C. elegans* locomotion is based on sinusoidal body undulations, body direction oscillates in small angles during locomotion. The movement time series was segmented into single swings for further analyses, with swing boundaries set at each peak of body direction oscillation (see Materials and Methods for details). In this study, a turn was judged based on the body shape as an instance where a part of the body (e.g., the head) touched or crossed another body part (e.g., the tail) (Figure 1D). For each swing, we determined whether the worm was moving forward or backward and whether the swing constituted a turn (i.e., a body touch occurred during the swing; see Materials and Methods for details). A total of 2411 turn blocks were detected.

### 2.2 | Turn Sequences Improve Movement Direction Through Ventral Rotation

To assess how turns affect worm orientation, we first examined changes in body direction caused by turns. Omega turns predominantly occur immediately after the transition from backward to forward locomotion, particularly following prolonged backward locomotion (Gray et al. 2005; Zhao et al. 2003). Additionally, multiple turns can occur before forward locomotion resumes. We therefore defined a “turn sequence” as a sequence of consecutive turn behaviors occurring between a backward locomotion and forward locomotion after the turns, and focused our analysis on such sequence events (Figure 2A). A total of 1440 turn sequences were detected. Orientation was assessed using *bearing*, defined as the

directional angle of the salt peak relative to the worm body direction vector (Figure 2B). The pre-bearing was defined as the average bearing of the last swing in backward locomotion before a turn sequence, while post-bearing was defined as the average bearing at the first swing in forward locomotion after the turn sequence (Figure 2C, top).

The mean pre-bearing of all turn events was  $-163.6^\circ$  (standard deviation,  $128.4^\circ$ ) (Figure 2D), and the mean post-bearing was  $34.2^\circ$  (standard deviation,  $133.6^\circ$ ) (Figure 2F). The  $\Delta$ -bearing, defined as post-bearing – pre-bearing, which is close to  $-1 \times$  rotation angle of the worm, had an average of  $-163.3^\circ$  (standard deviation,  $82.0^\circ$ ) (Figure 2E). Overall, the results indicate that turn sequences tended to occur when the worm was facing away from favorable salt concentrations, and after turn sequences, it was more likely to be oriented toward the favorable direction. The distribution of cumulative rotational angles (see Materials and Methods) was predominantly positive, with a mean of  $162.2^\circ$ . Some turn sequences involved rotations exceeding  $360^\circ$ , indicating that turn sequences generally caused rotation toward the ventral side (standard deviation,  $83.2^\circ$ ) (Figure 2G).

### 2.3 | The Turning Angle, Rather Than Occurrence Probability, of Turn Sequences Is Regulated Depending on Chemical Gradient

As described above, turns contribute to chemotaxis (Jang et al. 2019). Because the bearing distribution prior to the turn sequence (pre-bearing) is biased away from the favorable direction (Figure 2D), and worms rotate by about half a circle during the turn sequence (Figure 2E), this bias alone could sufficiently account for the contribution of turn sequences to chemotaxis. This bias of pre-bearing can be explained by previously reported trends: the pirouette behavior, which often begins with a reversal, is more likely to occur when the worm is oriented away from the salt peak (Pierce-Shimomura et al. 1999), and a reversal is more likely to be followed by a sequence of turns (Gray et al. 2005; Zhao et al. 2003). However, in this context, two additional mechanisms may also be involved: worms may actively regulate (i) the probability of turn sequence occurrence and (ii) fine-tuning of turning angles within turn sequences, to achieve better orientation after the turn sequence. We therefore investigated whether each of these two factors is regulated depending on the salt concentration gradient (bearing) prior to the turn sequence.

First, we examined whether the probability of occurrence of turn sequences is regulated. As mentioned above, we focus on turn sequences that occur following backward locomotion. We compared the bearing of two types of events following backward locomotion: one in which the worm turned, and another in which it switched back to forward locomotion without turning.

Specifically, we compared the distribution of the bearing before the turn (pre-bearing with turns) and the distribution of the bearing before the switch to forward locomotion without turns (pre-bearing without turns) (Figure 2C). The distributions of the pre-bearing with turns and pre-bearing without turns were similar, with comparable mean angles of  $-163.6^\circ$  and  $-157.6^\circ$ , respectively (Figure 2H, left). This trend is also reflected in the

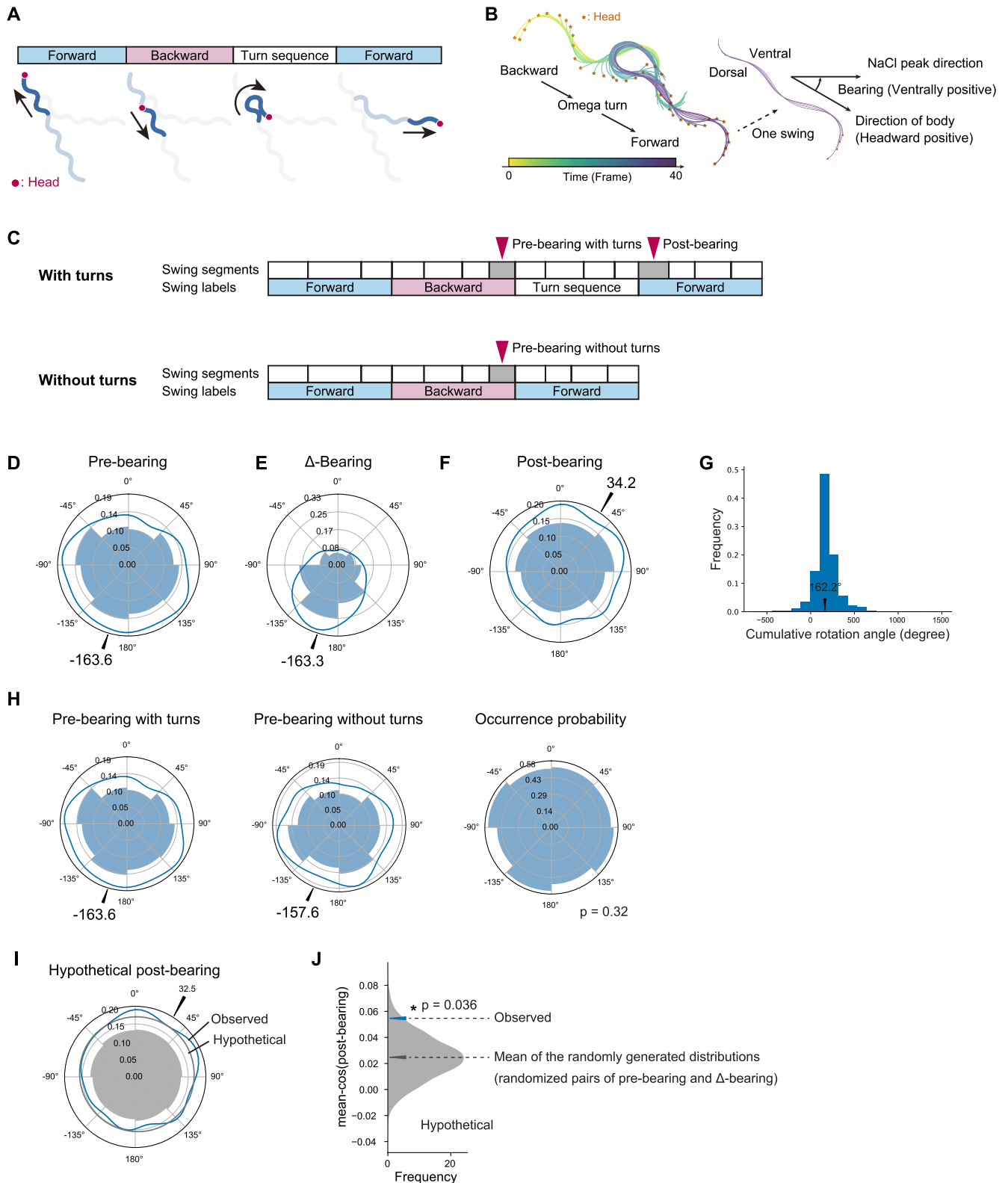


**FIGURE 2** | Legend on next page.

even distribution of the occurrence probability of turns per pre-bearing bin (i.e., the ratio of the number of backward locomotion followed by turns versus total number of backward locomotion, in each pre-bearing bin) (Figure 2H, right). The distribution of turn occurrence did not significantly differ depending on

pre-bearing bins ( $\chi^2 = 8.14$ ,  $df = 7$ ,  $p = 0.32$ , chi-square test of independence). Thus, we found no evidence that the initiation of the turn sequence is regulated based on the bearing at the point of transition from backward locomotion to turn or forward locomotion.

**FIGURE 2** | The turning angle of turn sequences are regulated depending on chemical gradient. (A) Schematic drawing of a turn sequence. In this study we focused on turn sequences after the transition from forward to backward locomotion. Turns were defined as Figure 1D. Forward locomotion follows the end of the turn sequence. (B) Example of a turn and determination of bearing. (left) A sequence of worm centerlines showing backward locomotion, a turn and forward locomotion, was color-coded, with the head marked by orange dots. The bearing was defined for each swing. The direction of the worm was determined by averaging the segment angles of the centerline, and the direction of NaCl peak relative to the worm direction, ventral side positive, was determined as bearing. (C) A sequence with/without turns. For regular turn sequence (top) pre-bearing and post-bearing were defined as in Figure 2B at the last swing of backward locomotion before the turn sequence and the first swing of forward locomotion after the turn sequence, respectively. The pre-bearing without turns was similarly defined in case no turn followed the backward locomotion (bottom). (D–F) Distribution of pre-bearing (D),  $\Delta$ -bearing (E), and post-bearing (F).  $\Delta$ -bearing is the difference between pre-bearing and post-bearing. Histograms (bars) in 45° bins, kernel density estimation of the distribution (blue lines), and average angle (arrowhead), are shown for each plot. (G) Histogram of cumulative rotation angle (see Materials and Methods). Animals rotate to the ventral side in most cases and the maximum cumulative rotation angle can exceed 360°. (H) Distribution of pre-bearing with turns (same as (D)) (left) or without turns (center). The chi-square test revealed no significant difference of occurrence probability (right) depending on pre-bearing ( $\chi^2 = 8.14$ ,  $df = 7$ ,  $p = 0.32$ ). (I) Distribution of hypothetical post-bearing generated using the randomized pairs of pre-bearing and  $\Delta$ -bearing (gray bars and line), with overlaid kernel density estimation of actual post-bearing (blue, same as F). (J) Bootstrap distribution of the mean-cos(post-bearing) of hypothetical post-bearing (gray) and the actual mean-cos(post-bearing) (blue arrowhead).

Next, to investigate whether the turning angle is regulated, we tested whether  $\Delta$ -bearing (post-bearing – pre-bearing) was determined independent of the bearing before the start of the turn sequence (pre-bearing) or depended on pre-bearing.

To test this, we employed a bootstrapping approach. Given that the post-bearing is calculated as the sum of the pre-bearing and the  $\Delta$ -bearing, we generated a hypothetical post-bearing distribution by randomly pairing values from the distributions of pre-bearing and  $\Delta$ -bearing and summing each pair (Pierce-Shimomura et al. 1999; Jang et al. 2019). In this procedure, the original distributions of both pre-bearing and  $\Delta$ -bearing were preserved. We then compared the simulated distribution of post-bearing with the actual post-bearing (Figure 2I). If the  $\Delta$ -bearing were not regulated based on the pre-bearing, the distribution of the hypothetical post-bearing would be indistinguishable from that of the empirically observed post-bearing. Although the hypothetical post-bearing had a mean of 32.5°, nearly identical to that of the actual post-bearing (34.2°), it was more evenly distributed than the actual post-bearing. To evaluate the distribution of post-bearing, we compared the mean of cos(post-bearings), the component of the worm orientation vector toward the salt peak (the closer the worms are oriented toward more favorable salt concentrations, the larger are the values). The actual value of mean-cos(post-bearing) showed a significantly higher score compared to the randomly generated distributions (Figure 2J). This suggests that the turning angles are not random but are regulated depending on the bearing before the turn sequence (pre-bearing). These results indicate that worms actively regulate their turning angles during the turn sequences of omega/delta turns based on their orientation before the turn, effectively adjusting their direction relative to the salt concentration peak.

## 2.4 | Visualization and Classification of Turn Sequences

How, then, are the turning angles regulated? It could be achieved by regulating the deepness of a single turn or by selecting turn types such as omega and delta turns. Otherwise, it could involve a combination of consecutive turns. To investigate this, we first examined the variation of turns by analyzing

the postural dynamics during turn sequences, using the same dataset described earlier in this paper. As described in Materials and Methods, the instantaneous posture of *C. elegans* is represented as a vector of angles of centerline segments relative to the coordinate axis, with the ventral side defined as positive. To overview the repertoire of posture patterns, each turn sequence was represented as a sequence of posture vectors, forming a high-dimensional vector, which was projected onto a t-SNE map (see Materials and Methods for details). For this mapping, worms' initial orientations were aligned to zero degrees (along the x-axis). When worms' rotation angles were color-coded on the t-SNE map, this feature appeared as a gradient along one dimension (Dimension 1) of t-SNE (Figure 3A). This is reasonable since the final orientation of the worm corresponds closely to the rotation angle given that the initial orientation was aligned. On the other hand, the turn sequence length (turn duration) did not align with either axis (Figure S2).

We further examined the direction of worm movement (forward or backward) during turn sequences. This analysis revealed that contrary to previous assumptions that turns occur only during forward movement (Gray et al. 2005; Zhao et al. 2003), turns (defined by body contact) also occurred during backward movement. We therefore classified turns (body contact events) based on the direction of worm movement during body contact: “F” turns if body contact occurred during forward movement (an example shown in Figure 3B), and “B” turns if it occurred during backward movement (Figure 3D). Additionally, some worms exhibited transitions from backward to forward movement during body contact (“BF” turns) (Figure 3C). In standard forward F turns, a worm's head typically contacted its ventral side, whereas in most turns that occurred during backward movement (B turns), body contacts mostly happened on the dorsal side. Quantification of the proportion of each turn type classified based on forward/backward movement showed that 59.8% were forward turns (F), 26.5% were backward turns (B), and the remaining turns, which involved transitions between backward and forward movements, occurred less frequently (Figure 3G).

Turn sequences, which were defined as continuous turns occurring between a backward locomotion and forward locomotion after the turns, can consist of single turns, or double or



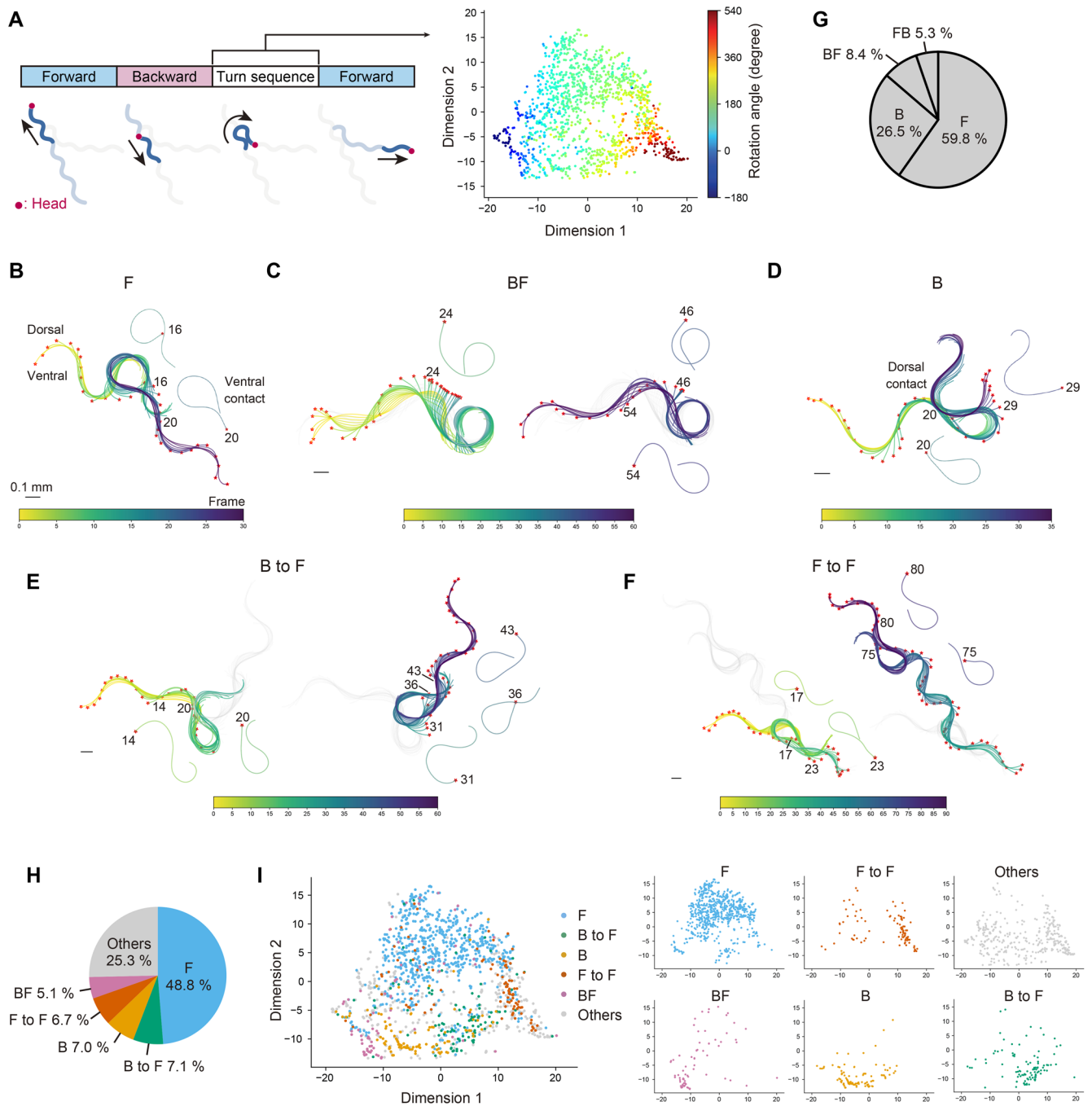


**FIGURE 3 | Diversity of turn sequences.** (A) t-SNE representation of the posture dynamics during turn sequences. A sequence of centerline shapes during the turn sequence was assembled as a vector and displayed in a t-SNE map. The cumulative turning angle of each turn sequence was color-coded. (B–F) Examples of centerline shape for each turn sequence type, F (B), BF (C), B (D), B to F (E), and F to F (F). Time is color-coded, and the numbers indicate the time points. Several time points are shown extracted as insets. In BF, B to F and F to F, the sequence was split into first and second half for convenience of viewing. (G) Ratio of each type of turn (F: Forward, B: Backward, BF: Backward then forward, FB: Forward then backward) among all turns. (H) Ratio of sequence types among all turn sequences (F: A single forward turn, B: A single backward turn, BF: A single turn with backward to forward switch, B to F: A backward turn followed by a forward turn, F to F: A forward turn followed by another forward turn). (I) (left) The same t-SNE map as in (A), (right), color-coded by turn sequence types categorized as in (H). (right) Separate t-SNE plots of each turn sequence type.

multiple consecutive turns. Turn sequences were classified based on the sequence of turn types, F, B, BF, or FB. As a result, the five most frequent turn sequence types were as follows: 48.8% of all turn sequences were single forward turns (F). The next three most common types were a backward turn followed by a forward turn (B to F), a single backward turn

(B), and two consecutive forward turns (F to F), each consisting of about 7%. Lastly, about 5% consisted of a single turn beginning with a backward movement and ending with a forward movement (BF) (Figure 3H). Mapping these five most frequent sequence types onto the t-SNE plot revealed that the turn distribution on t-SNE was divided into two halves along

the second t-SNE axis (Dimension 2), with the upper half of the plot containing sequences composed of one or two forward turns (F, F to F) and the lower half comprising other types of turn sequences (Figure 3I). In the lower half, sequence types were arranged along the first axis in the order of BF, B, B to F, and F to F. This suggests that turn sequence types differ in rotation angles and that there are two distinct strategies for achieving similar rotation angles.

To visualize actual behaviors, we plotted representative postural dynamics for the five most frequent turn sequence types (Figure 3B–F, Supporting Information Movies S1, see Materials and Methods for details). The postural dynamics were highly diverse, including variations in body shape when the head contacted the body, diversity in head movements during forward movement after a turn, and differences in rotation angles during each behavior.

## 2.5 | Contribution of Turn Sequence Type Selection and Turning Angle Adjustment to Adjustment of Turning Angles

How is this behavioral repertoire utilized for adjusting turning angles? To answer the question, we first plotted the distributions of pre-bearing,  $\Delta$ -bearing, and post-bearing for each sequence type (Figure 4A). The distribution of turning angle ( $\Delta$ -bearing) was highly biased in some sequence types. For instance, in F turns,  $\Delta$ -bearing had a narrow distribution around  $-160^\circ$ , indicating that once an F turn occurred, the worm rotated so as to finally face nearly the opposite direction. This distribution showed minimal overlap with that of B to F turns, demonstrating the qualitative difference between these behaviors. On the other hand, some turns such as BF and B had a wider distribution of  $\Delta$ -bearing. These observations raise the possibility that either or both the selection of sequence type and adjustment of turning angle within a single sequence type could contribute to the regulation of overall turning angles.

To see whether the occurrence of each sequence type is regulated based on pre-bearing, we compared the distribution of pre-bearing across the five sequence types. The frequency of occurrence of each of the five sequence types significantly differed between bearing angle bins ( $\chi^2 = 29.20$ ,  $df = 12$ ,  $p = 3.7 \times 10^{-3}$ , chi-square test) (Figure 4B). This result supports the hypothesis that worms select the sequence types based on bearing before the turn sequence.

Next, to assess whether adjustment of turning angles within a single sequence type contributes to the selection of proper turning angles, we shuffled the correspondence between pre-bearing and  $\Delta$ -bearing for each sequence type and generated hypothetical distributions of post-bearing based on the assumption of independence of  $\Delta$ -bearing and pre-bearing (called intra-type randomization). The results showed that in the B to F sequence type, the mean of  $\cos(\text{post-bearing})$  was significantly higher than those expected under the independence assumption. In contrast, directionality in other types of turn sequences was not significantly different from the randomized distribution (Figure 4C). This suggests that in B to

F turn sequences, turning angles are adjusted depending on pre-bearing to better orient the animals toward the preferred direction, whereas this type of adjustment was not evident for other turns. Next, to test whether the selection of sequence types contributes to the adjustment of turning angles, we shuffled the correspondence between pre-bearing and  $\Delta$ -bearing across different sequence types (called inter-type randomization). For instance, for “F” in Figure 4D,  $\Delta$ -bearing values sampled from either BF, B, B to F, or F to F turns were combined with the pre-bearing of F turns. Compared to this randomized distribution, actual post-bearing for the F turns had a significantly higher mean- $\cos(\text{post-bearing})$  value. To further clarify the roles of sequence type selection, we took all turn sequences (as in Figure 2J), but this time shuffled only single turns (F, B and BF) in two ways. When pre-bearing:  $\Delta$ -bearing pairs were randomized across different sequence types (inter-type randomization), the mean- $\cos(\text{post-bearing})$  was significantly higher than that of the randomized distribution (Figure 4E). When pre-bearing:  $\Delta$ -bearing pairs were randomized within each sequence type (intra-type randomization), no significant discrepancy was found (Figure 4F). Therefore, for single turns, selecting the appropriate sequence type is crucial for improving post-turn orientation. Randomization across all five types also revealed a significant bias of post-bearing (Figure 4G).

Collectively, these findings indicate that turning angle regulation is achieved in a two-step process: (1) selection of the sequence type (at least in the case of single turns) and (2) adjustment of the turning angle within the selected sequence type (for the B to F turns). The combination of these regulatory mechanisms across different types of turn behaviors enables the worms to turn to a better orientation and fulfill efficient chemotaxis.

## 3 | Discussion

In the study of chemotaxis in *Caenorhabditis elegans*, two major behavioral mechanisms have been identified: the pirouette mechanism and the weathervane mechanism. Initially, the pirouette mechanism was not considered to include turning angle regulation. However, as suggested when the pirouette mechanism was first reported (Pierce-Shimomura et al. 1999) and later rediscovered (Jang et al. 2019), the adjustment of reorientation angles contributes to efficient chemotaxis using pirouettes. Since a pirouette consists of a series of sequential behaviors including reversals and various types of turns, understanding how the reorientation angle is regulated within a pirouette required a detailed analysis of its component behaviors.

Previous studies investigating the reorientation angle regulation in pirouettes have primarily relied on centroid data (Tanimoto et al. 2017; Jang et al. 2019). In this study, in contrast, we extracted centerlines from high-resolution worm images, enabling more accurate classification of turning behaviors. Additionally, by using transgenic strains with fluorescently labeled head, side, and ventral regions, we could assign both anteroposterior and dorsoventral axes to the worms. This was crucial because worms lie on either side of

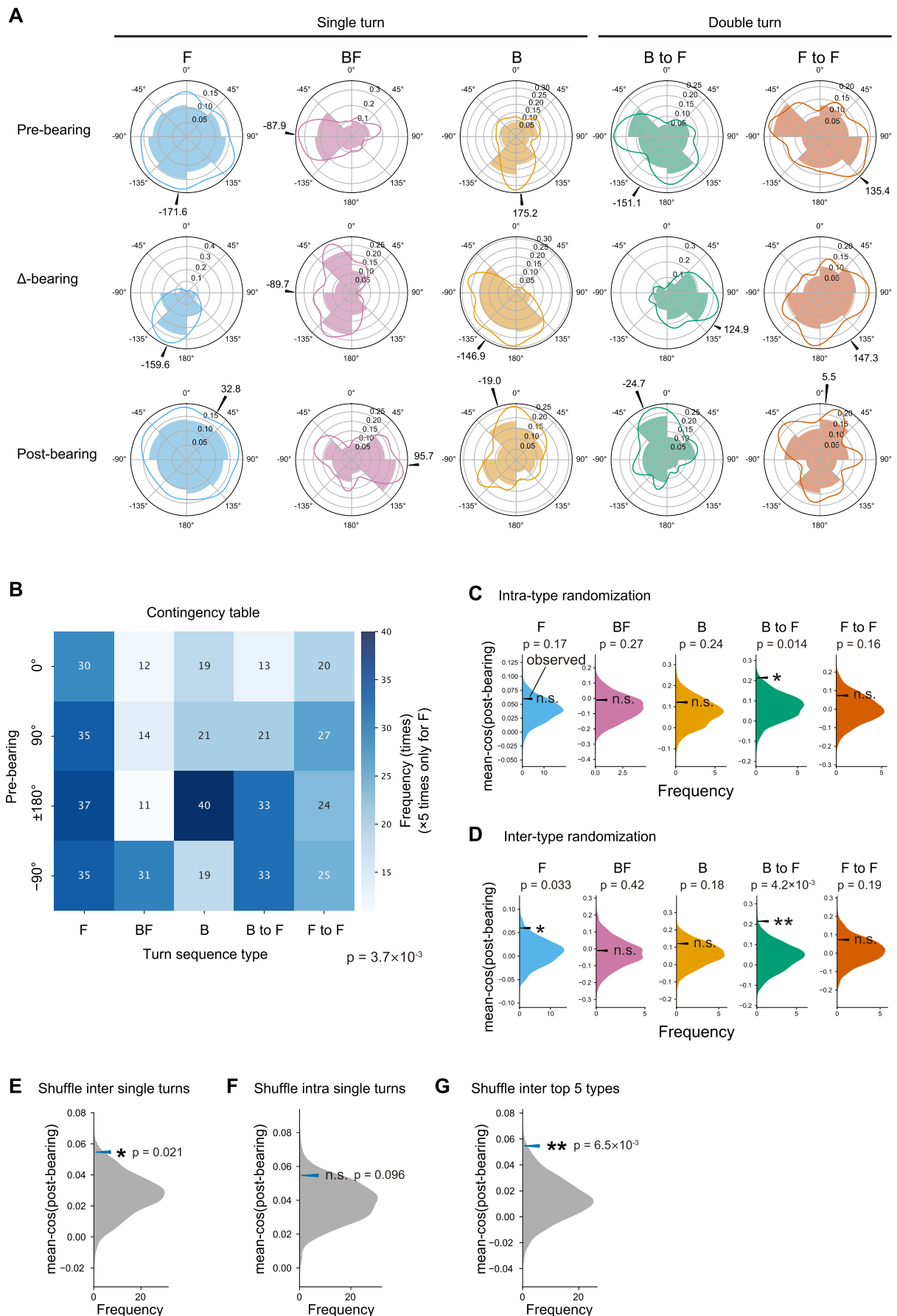


**FIGURE 4** | Legend on next page.



**FIGURE 4** | Turn Sequence type selection and turning angle adjustment. (A) Distribution of pre-bearing,  $\Delta$ -bearing and post-bearing for each turn sequence type. See Figure 2D–F for description. (B) Contingency table of pre-bearing segmented into 90° bins and turn sequence type. The chi-square test revealed significant relationship between the bearing categories (divided into four bins) and the turn sequence types ( $\chi^2 = 29.20$ ,  $df = 12$ ,  $p = 3.7 \times 10^{-3}$ ). (C) Distribution of hypothetical mean-cos(post-bearing), of the randomized post-bearing and actual mean-cos(post-bearing) (arrowhead) for each turn sequence type. Pairs of pre-bearing and  $\Delta$ -bearing were randomized in each sequence type. (D) Distribution of hypothetical mean-cos(post-bearing) and actual mean-cos(post-bearing) (arrowhead), for each turn sequence type. In contrast to (C),  $\Delta$ -bearing was taken from other four sequence types for randomization. (E–G) Distribution of mean-cos(bearing) of hypothetical post-bearing and actual mean-cos(post-bearing) of all turn sequences, where randomization was performed by taking  $\Delta$ -bearing from other two of the three single sequence types (F, B and BF) (E), or from each single sequence type (F), or from other four sequence types (G). In (C–G), one-sided z-tests were performed with the null hypothesis that the actual score is a sample from the randomized distribution.

the body on the agar surface and therefore the movement is asymmetrical. In fact, the distribution of rotation angles in the turn sequences was highly skewed toward positive values, with a mean of approximately 160° (Figure 2G), indicating that most turns resulted in ventral-side rotation. Therefore, evaluating turn rotation angles based on the dorsoventral axis of the worm, rather than absolute plate coordinate-based rotation angles, provided a clearer description of turn direction bias. Furthermore, this fluorescence labeling system allowed us to define axial orientation in centerline-based posture measurements, enabling a more detailed analysis of body postures. We need to be cautious that it is possible that genetic modifications or exposure to excitation light may have increased the turn frequency compared to the natural environment. Nevertheless, even under the imaging conditions used in this study, chemotactic behavior was still observed, allowing us to extract all behaviors that can contribute to efficient chemotactic migration (Figure 1B).

This study focused on turn sequences, which involve significant posture changes within a pirouette, and demonstrated that the turning angles, rather than occurrence probability, of turn sequences are regulated depending on the bearing of chemical stimulus before the sequence. Furthermore, the classification of turn sequences revealed that, for a certain sequence type, turning angles are regulated within the type, and that the selection of specific sequence types at the initiation of turns contributes to directional improvement. It is important to note, however, that this selection is probabilistic and not perfectly accurate. Regarding turns initiated by backward movement, no turning angle regulation was detected regardless of whether the turn ended in forward or backward movement. Therefore, turn sequences containing forward-directed turns appear to be the most effective in improving directional navigation.

The observations in this study revealed previously unrecognized layers of behavioral adjustment for efficient chemotaxis. In previous studies, pirouettes have been regarded merely as prolonged sets of complex behaviors. However, in this study, we have successfully decomposed them into their constituent behavioral elements. Furthermore, by categorizing turn sequences into distinct types, we have revealed that the sequence type is selected according to the pre-bearing angle before the turn sequence occurs. This finding raises further questions about how such control is achieved. Each behavioral sequence is a chronological combination of different movements, such as forward/backward movements, ventral bending, and dorsal bending. It

is noteworthy that the worms' nervous system can create the behavioral program for each type, and the neural mechanisms that generate these multiple different programs need to be elucidated in future studies. Previous studies revealed that the timing of the motor sequence of backward and turning behaviors can be flexibly orchestrated by inhibitory interactions between motor modules (Wang et al. 2020). Other studies revealed that the deepness of body bends can be modulated by neuropeptides or neurotransmitters that act on motor neurons and body muscles (Donnelly et al. 2013; Florman and Alkema 2022). These findings from previous studies provide potential insights into the neural mechanisms underlying the control of these turn sequences. Furthermore, the timescale of the turn sequences that we identified aligns with previously proposed nested neuronal dynamics and the associated hierarchical temporal structure of behavior (Kaplan et al. 2020), supporting the idea that elucidating the control mechanisms at this layer may contribute to a better understanding of how neuronal dynamics implement behavioral hierarchy.

As mentioned earlier, worms perform chemotaxis by sensing salt concentration with a sensory organ located at a single point on their head. They therefore need to calculate the salt gradient based on the changes in sensory input through limited movement over a short time and distance. While the weathervane mechanism and the pirouette mechanism can be explained by immediate and reflexive responses at any given moment (Iino and Yoshida 2009; Pierce-Shimomura et al. 1999; Matsumoto et al. 2024), the turn behaviors revealed in this study suggest that the calculated salt concentration gradient needs to be stored as an internal state, and this information must be reflected in the selection of the behavioral sequence type. Therefore, elucidating the neural mechanism for such calculation is highly desired. In addition, the depth of the turn ( $\Delta$ -bearing) is adjusted in a turn sequence type, and in this case it is necessary to clarify at which time point the salt gradient is sensed and reflected in the adjustment of turn depth. Observing neural activities using calcium and voltage sensors in moving animals will be a powerful approach to identify neurons relevant to the regulation of these behaviors. Additionally, to achieve temporal resolution in understanding sensory regulatory mechanisms, perturbation techniques such as optogenetics will be useful in future studies.

More broadly, the behavioral analysis framework employed in this study has the potential to contribute to comparative research on navigation strategies across various animal species, including not only *C. elegans* but also birds and fish (Demšar et al. 2025; Rodríguez et al. 2021).

## 4 | Experimental Procedures

### 4.1 | Worm Culture and Strains

*C. elegans* was cultured at 20°C on Nematode Growth Medium (NGM) plates containing 50 mM of NaCl, with *Escherichia coli* NA22 as a food source. We used JN2824 (N2; Ex[pCFJ104(Pmyo-3::mCherry)+pPD49.26]). In this strain, body-wall muscles located all along the periphery of the body and egg-laying muscles at the ventral side of the midbody are marked with mCherry fluorescence.

### 4.2 | Chemotaxis Assays

To quantify the behavior of *C. elegans* on a chemical gradient, we performed a salt chemotaxis assay basically as previously described (Kunitomo et al. 2013; Tomioka et al. 2016), with a total of 99 animals. Adult hermaphrodites were washed from growth plates in KP25 buffer (25 mM potassium phosphate, pH 6.0, 1 mM CaCl<sub>2</sub>, 1 mM MgSO<sub>4</sub>, 50 mM NaCl) and conditioned for 6 h on 5 cm NGM plates containing 100 mM NaCl with NA22 as a food source. After the conditioning, individual animals were picked and transferred to the center of a 9 cm plate with a salt gradient ranging from ~35 to ~95 mM (Kunitomo et al. 2013), and allowed to crawl freely for 15 min. Under these conditions, animals show migration bias toward high salt concentrations (Kunitomo et al. 2013; Luo et al. 2014b).

### 4.3 | Tracking Imaging

Time-lapse fluorescence and bright-field images were simultaneously acquired using a customized upright microscope (BX51, Olympus). The microscope was equipped with an LMPLFLN 5× objective lens, U-MF2 filter cube with a dichroic mirror (FF493/574-Di01, Semrock) and an excitation filter (FF01-468/553, Semrock), and an additional dichroic mirror (DM690) that splits the light paths for infrared and fluorescence images. The fluorescence images were acquired at five frames per second using an ImagEM EM-CCD camera (C9100-13, Hamamatsu) with an IR-cut filter and an emission filter (FF01-617/73, Semrock), under an excitation light intensity of 0.27 mW/mm<sup>2</sup>. Bright-field images to monitor animal movement were captured at 33 frames per second using near-infrared illumination from an IR lamp at an intensity of 0.09 mW/mm<sup>2</sup> and an infrared camera (GRAS-03K2MC, Point Gray Research). The microscope setup was equipped with an XY motorized stage (Hawkvision) for precise tracking along the X and Y axes. Image acquisition and stage movements were controlled by a custom software, which processed the bright-field images to maintain the animal within the microscope's field of view.

Since *C. elegans* lies on its side on the agar surface, some animals lie with their left side down and others with their right side down. Therefore, dorso-ventral orientation of each worm was visually scored based on the location of egg-laying muscles and used to adjust the rotation directions as worm-centered for later analyses.

The correspondence between the time stamps of bright-field and fluorescence images were determined by matching the stage coordinates with the animal movement estimated from the centerline extracted from fluorescence images (see the “Estimation of centroid movement from centerlines” section for details).

### 4.4 | Centerline Extraction

To extract worm centerlines, fluorescence images were first binarized, and the silhouettes were skeletonized (Guo and Hall 1989; Lam et al. 1992) to generate a line passing through the body center. In extended postures, where different body parts do not contact each other, this line represents the actual centerline. However, in curled postures such as omega or delta turns, where different parts of the body contact each other, the centerline obtained by the skeletonization algorithm does not align well with the true centerline, making it impossible to obtain accurate centerlines using skeletonization alone.

Therefore, for curled postures, centerlines were determined using a modified version of WormTracer (Kuze et al. 2023). WormTracer simultaneously optimizes the centerlines in consecutive frames by incorporating constraints on the temporal continuity of posture dynamics and the smoothness of the centerline while referring to the extended postures before and after the curled postures. Extracted centerlines were then visually inspected by overlaying them onto silhouettes, and any incorrect centerlines were manually redrawn to pass through the actual body center (Figure 1C).

The centerline was represented by 100 junction points, forming 99 equal-length line segments from head to tail. The animal's posture and position were described by the angles of the segments relative to the coordinate axis and the coordinates of the centroid of junction points.

### 4.5 | Definition of Omega/Delta Turns

Omega turns involve body bends where the head touches the body without crossing over, while delta turns involve the head crossing the body (Croll 1975; Gray et al. 2005; Broekmans et al. 2016). However, we realized that there are intermediate cases where the head temporarily crossed over the body, then slid along the body, and returned to the original side without landing on the other side. Therefore, it is difficult to clearly distinguish omega turns from delta turns, and both were analyzed collectively as “turns”. In this study, turns were defined based on centerline data as postures in which a body part contacts another body part (Figure 1D).

### 4.6 | Analysis of Turning Angle Regulation

Using centerline segments angles, mean angles were calculated at each time point. The vector pointing toward the worm's head in this mean angle was considered the body direction. The angle between the body direction vector and the vector pointing from the position of the worm to the NaCl

concentration peak defined as bearing. Thus, bearing of  $0^\circ$  indicates the worm is heading straight toward the salt peak, while  $\pm 180^\circ$  indicates a heading away from the peak. The sign of the bearing angle was set so that the rotation of the worm head toward the ventral side is positive (Figure 2B). The circular mean and standard deviation of the bearings were calculated as follows. For each angle  $\theta_i$ , its Cartesian components were determined:  $x_i = \cos \theta_i$  and  $y_i = \sin \theta_i$ . The mean Cartesian components were then computed:  $\bar{x} = \frac{1}{n} \sum_{i=1}^n x_i$  and  $\bar{y} = \frac{1}{n} \sum_{i=1}^n y_i$ . The circular mean angle  $\bar{\theta}$  was determined as the argument of the mean resultant vector  $(\bar{x}, \bar{y})$ , yielding a value in the range  $[-\pi, \pi]$  radians. This angle represents the signed angle, measured counterclockwise from the positive x-axis to the direction of the vector  $(\bar{x}, \bar{y})$ . The mean resultant length  $R = \sqrt{\bar{y}^2 + \bar{x}^2}$  was used to calculate the circular standard deviation  $s = \sqrt{-2 \ln R}$ . All calculations were performed using radians as the unit for angles, and the final mean angle and standard deviation were converted to degrees for reporting in the manuscript.

Because *C. elegans* exhibits sinusoidal locomotion, body direction oscillates during forward or backward locomotion, while during turns, the body direction typically rotates in either the positive or negative direction. To quantify chemotaxis behaviors, we processed the data as follows:

#### 4.6.1 | Swing Segmentation

Worm movement was segmented into swings based on body direction oscillation, with swing boundaries set at each peak of body direction change.

#### 4.6.2 | Swing Labeling

Each swing was labeled as forward or backward based on the movement direction (see below for details), and also as whether a turn (as defined above) occurred or not.

#### 4.6.3 | Turn Sequence

For turn sequence analysis (Figures 2–4, described in detail in the following sections), a turn was defined as a sequence of consecutive swings labeled as turns. Then, a “turn sequence” was defined as a sequence of consecutive turn behaviors occurring between a backward locomotion and forward locomotion after the turns, and focused our analysis on such sequence events. The mean bearing during the last backward swing before the turn sequence (pre-bearing) and the mean bearing during the first forward swing after the turn sequence (post-bearing) were compared.  $\Delta$ -bearing was determined simply by subtracting pre-bearing from post-bearing. All angles were expressed in degrees between  $-180^\circ$  and  $180^\circ$ , except for the cumulative rotation angle, which represented the sum of directional changes between consecutive time points.

To analyze the regulation of turning angle, we performed a permutation test followed by a Z-test to compare the

mean-cos(bearing) of actual post-bearing with the distribution of mean-cos(bearing) of the hypothetical post-bearing. The hypothetical post-bearing was calculated by shuffling the  $\Delta$ -bearing values across trials and adding them to the pre-bearing values.

### 4.7 | Analysis of Occurrence Probability Regulation

In the analysis of the regulation of occurrence probability, we performed a chi-square test to see whether the occurrence of turn sequence or the occurrence of five types of turn sequences is distributed differently between different bins of pre-bearing or is independent of pre-bearing.

### 4.8 | Dissection of Turn Sequence by t-SNE

As described earlier, the centerline information at each time point is represented by a vector of 99 segment angles (designated  $\theta_{t,i}$  where  $t$  is time and  $i$  is the segment number 1, 2, ..., 99). To visualize the diversity of turn sequence behaviors, for each turn sequence (consecutive swing including turn events), we extracted a time span from the midpoint of the last swing in backward locomotion before the turn sequence ( $t_{start}$ ) to the midpoint of the first swing in forward locomotion after the turn sequence ( $t_{end}$ ). From each set of  $\theta_{t,i}$  ( $t = t_{start}, \dots, t_{end}$ ), a constant was subtracted to make  $\text{mean}(\theta'_{t,i}) = 0$ . Because the time spans are of various lengths, the adjusted  $\theta'_{t,i}$  ( $t = t_{start}, \dots, t_{end}$ ) was transformed to 30  $\theta'_{t,i}$  vectors by linear interpolation of the time dimension. The resulting  $30 \times 99$  matrices were then flattened into vectors of length 2970 and subjected to two-dimensional t-SNE.

### 4.9 | Estimation of Centroid Movement From Centerlines

Due to the lack of synchronization between the stage controller and image acquisition software in our imaging setup, we needed to match the timestamps of these controllers. To achieve this, we estimated centroid movement solely from the centerline time series obtained from the images. The resistive force acting on each segment of the worm from the substrate is composed of components normal and tangent to the segment as follows:

$$\begin{aligned} \mathbf{F}_i &= r_i \mathbf{v}_i (\mathbf{v}_i \cdot \Delta \mathbf{x}_i) + \mu_i \lambda_i (\lambda_i \cdot \Delta \mathbf{x}_i) \\ &= r_i \mathbf{v}_i \left\{ \mathbf{v}_i \cdot (\Delta \mathbf{x}^{(c)} + \Delta \mathbf{x}_i^{(r)}) \right\} + \mu_i \lambda_i \left\{ \lambda_i \cdot (\Delta \mathbf{x}^{(c)} + \Delta \mathbf{x}_i^{(r)}) \right\} \\ &= r_i (\mathbf{v}_i \mathbf{v}_i^T) (\Delta \mathbf{x}^{(c)} + \Delta \mathbf{x}_i^{(r)}) + \mu_i (\lambda_i \lambda_i^T) (\Delta \mathbf{x}^{(c)} + \Delta \mathbf{x}_i^{(r)}) \end{aligned}$$

where  $\Delta \mathbf{x}_i$  is the movement vector of the midpoint of  $i$ 'th centerline segment during a short interval ( $\Delta t$ ), which can be decomposed to the movement vector of the centerline centroid,  $\Delta \mathbf{x}^{(c)}$ , and movement of each centerline segment midpoint relative to the centroid,  $\Delta \mathbf{x}_i^{(r)}$ .  $r_i$  and  $\mu_i$  are the friction coefficients normal and tangential to the  $i$ 'th segment, respectively;  $\mathbf{v}_i$  and  $\lambda_i$  are the unit vectors normal and tangential to the  $i$ 'th segment, respectively.

According to the resistive force theory (Keaveny and Brown 2017), translation of the worm during a short interval  $\Delta t$  is equivalent to the amount that makes the sum of  $F_i$  zero.

$$\sum_i F_i = 0$$

Solving the equation yields:

$$\begin{bmatrix} \Delta x^{(c)} \\ \Delta y^{(c)} \end{bmatrix} = - \begin{bmatrix} \sum_{i=0}^{M-1} (r_i v_{x,i} v_{x,i} + \mu_i \lambda_{x,i} \lambda_{x,i}) & \sum_{i=0}^{M-1} (r_i v_{y,i} v_{x,i} + \mu_i \lambda_{y,i} \lambda_{x,i}) \\ \sum_{i=0}^{M-1} (r_i v_{x,i} v_{y,i} + \mu_i \lambda_{x,i} \lambda_{y,i}) & \sum_{i=0}^{M-1} (r_i v_{y,i} v_{y,i} + \mu_i \lambda_{y,i} \lambda_{y,i}) \end{bmatrix}^{-1} \begin{bmatrix} \sum_{i=0}^{M-1} \left\{ (r_i v_{x,i} v_{x,i} + \mu_i \lambda_{x,i} \lambda_{x,i}) \Delta x_i^{(r)} + (r_i v_{y,i} v_{x,i} + \mu_i \lambda_{y,i} \lambda_{x,i}) \Delta y_i^{(r)} \right\} \\ \sum_{i=0}^{M-1} \left\{ (r_i v_{x,i} v_{y,i} + \mu_i \lambda_{x,i} \lambda_{y,i}) \Delta x_i^{(r)} + (r_i v_{y,i} v_{y,i} + \mu_i \lambda_{y,i} \lambda_{y,i}) \Delta y_i^{(r)} \right\} \end{bmatrix}$$

where  $\Delta \mathbf{x}^{(c)} = (\Delta x^{(c)}, \Delta y^{(c)})$ ,  $\Delta \mathbf{x}^{(r)} = (\Delta x^{(r)}, \Delta y^{(r)})$ . Suffices  $x$  and  $y$  on  $\mathbf{v}$  and  $\boldsymbol{\mu}$  denote the  $x$ - and  $y$ -components of each vector. Values  $\Delta x_i^{(r)}$ ,  $\Delta y_i^{(r)}$ ,  $v_{x,i}$ ,  $v_{y,i}$ ,  $\mu_{x,i}$ , and  $\mu_{y,i}$  were computed from the centerline segment angles at each time point. The time interval  $\Delta t$  was 1/100 of the time step of fluorescence images (2ms) and centerline data for each fraction time was deduced by linear interpolation. For simplicity, we put  $r_i = 1$ , and  $\mu_i = 0$  for all  $i$ , because this setting provided sufficiently accurate estimation (Figure S1).

Forward/backward movement estimation was performed based on  $\Delta \mathbf{x}^{(c)}$  and  $\Delta \mathbf{x}^{(r)}$  estimated as above. At three points along the body (head tip, tail tip, and midbody), the component of  $\Delta \mathbf{x}_i$  tangential to the centerline segment was calculated. The forward/backward worm movement label at each time point was determined by majority vote of the signs of these components.

## Acknowledgments

We thank our laboratory members for their helpful discussions and support.

## Conflicts of Interest

The authors declare no conflicts of interest.

## Data Availability Statement

The data that support the findings of this study are openly available in Turn\_Sequence\_chemotaxis at [https://github.com/KarinSuwazono/Turn\\_sequence\\_chemotaxis/tree/main](https://github.com/KarinSuwazono/Turn_sequence_chemotaxis/tree/main).

## References

- Albrecht, D. R., and C. I. Bargmann. 2011. "High-Content Behavioral Analysis of *Caenorhabditis elegans* in Precise Spatiotemporal Chemical Environments." *Nature Methods* 8: 599–605. <https://doi.org/10.1038/nmeth.1630>.
- Bell, W. J., and T. R. Tobin. 1982. "Chemo-Oriented." *Biological Reviews* 57: 219–260. <https://doi.org/10.1111/j.1469-185X.1982.tb00369.x>.
- Broekmans, O. D., J. B. Rodgers, W. S. Ryu, and G. J. Stephens. 2016. "Resolving Coiled Shapes Reveals New Reorientation Behaviors in *C. elegans*." *eLife* 5: e17227. <https://doi.org/10.7554/eLife.17227>.

Croll, N. A. 1975. "Components and Patterns in the Behaviour of the Nematode *Caenorhabditis elegans*." *Journal of Zoology* 176: 159–176. <https://doi.org/10.1111/j.1469-7998.1975.tb03191.x>.

Demšar, U., B. Zein, and J. A. Long. 2025. "A New Data-Driven Paradigm for the Study of Avian Migratory Navigation." *Movement Ecology* 13: 16. <https://doi.org/10.1186/s40462-025-00543-8>.

Donnelly, J. L., C. M. Clark, A. M. Leifer, et al. 2013. "Monoaminergic Orchestration of Motor Programs in a Complex *C. elegans* Behavior." *PLoS Biology* 11: e1001529. <https://doi.org/10.1371/journal.pbio.1001529>.

Florman, J. T., and M. J. Alkema. 2022. "Co-Transmission of Neuropeptides and Monoamines Choreograph the *C. elegans* Escape Response." *PLoS Genetics* 18: e1010091. <https://doi.org/10.1371/journal.pgen.1010091>.

Fraenkel, G. S., and D. L. Gunn. 1961. *The Orientation of Animals, Kineses, Taxes and Compass Reactions*. Dover Publications. <http://archive.org/details/AnimalOrientation>.

Gray, J. M., J. J. Hill, and C. I. Bargmann. 2005. "A Circuit for Navigation in *Caenorhabditis elegans*." *National Academy of Sciences of the United States of America* 102: 3184–3191. <https://doi.org/10.1073/pnas.04090910101>.

Guo, Z., and R. W. Hall. 1989. "Parallel Thinning With Two-Subiteration Algorithms." *Communications of the ACM* 32: 359–373. <https://doi.org/10.1145/62065.62074>.

Iino, Y., and K. Yoshida. 2009. "Parallel Use of Two Behavioral Mechanisms for Chemotaxis in *Caenorhabditis elegans*." *Journal of Neuroscience* 29: 5370–5380. <https://doi.org/10.1523/JNEUROSCI.3633-08.2009>.

Ikeda, M., S. Nakano, A. C. Giles, et al. 2020. "Context-Dependent Operation of Neural Circuits Underlies a Navigation Behavior in *Caenorhabditis elegans*." *National Academy of Sciences of the United States of America* 117: 6178–6188. <https://doi.org/10.1073/pnas.1918528117>.

Jang, M. S., Y. Toyoshima, M. Tomioka, H. Kunitomo, and Y. Iino. 2019. "Multiple Sensory Neurons Mediate Starvation-Dependent Aversive Navigation in *Caenorhabditis elegans*." *National Academy of Sciences of the United States of America* 116: 18673–18683. <https://doi.org/10.1073/pnas.1821716116>.

Kaplan, H. S., O. Salazar Thula, N. Khoss, and M. Zimmer. 2020. "Nested Neuronal Dynamics Orchestrate a Behavioral Hierarchy Across Timescales." *Neuron* 105: 562–576.e9. <https://doi.org/10.1016/j.neuron.2019.10.037>.

Keaveny, E. E., and A. E. X. Brown. 2017. "Predicting Path From Undulations for *C. elegans* Using Linear and Nonlinear Resistive Force Theory." *Physical Biology* 14: 025001. <https://doi.org/10.1088/1478-3975/aa5ce6>.

Kunitomo, H., H. Sato, R. Iwata, et al. 2013. "Concentration Memory-Dependent Synaptic Plasticity of a Taste Circuit Regulates Salt Concentration Chemotaxis in *Caenorhabditis elegans*." *Nature Communications* 4: 2210. <https://doi.org/10.1038/ncomms3210>.

Kuze, K., U. T. Tazawa, K. Suwazono, Y. Toyoshima, and Y. Iino. 2023. "WormTracer: A Precise Method for Worm Posture Analysis Using Temporal Continuity." *bioRxiv*. <https://doi.org/10.1101/2023.12.11.571048>.

Lam, L., S.-W. Lee, and C. Y. Suen. 1992. "Thinning Methodologies: A Comprehensive Survey." *IEEE Transactions on Pattern Analysis and Machine Intelligence* 14: 869–885. <https://doi.org/10.1109/34.161346>.

Luo, L., N. Cook, V. Venkatachalam, et al. 2014a. "Bidirectional Thermotaxis in *Caenorhabditis elegans* Is Mediated by Distinct Sensorimotor Strategies Driven by the AFD Thermosensory Neurons." *National Academy of Sciences of the United States of America* 111: 2776–2781. <https://doi.org/10.1073/pnas.1315205111>.



Luo, L., Q. Wen, J. Ren, et al. 2014b. “Dynamic Encoding of Perception, Memory, and Movement in a *C. elegans* Chemotaxis Circuit.” *Neuron* 82: 1115–1128. <https://doi.org/10.1016/j.neuron.2014.05.010>.

Matsumoto, A., Y. Toyoshima, C. Zhang, A. Isozaki, K. Goda, and Y. Iino. 2024. “Neuronal Sensorimotor Integration Guiding Salt Concentration Navigation in *Caenorhabditis elegans*.” *National Academy of Sciences of the United States of America* 121: e2310735121. <https://doi.org/10.1073/pnas.2310735121>.

Pierce-Shimomura, J. T., T. M. Morse, and S. R. Lockery. 1999. “The Fundamental Role of Pirouettes in *Caenorhabditis elegans* Chemotaxis.” *Journal of Neuroscience* 19: 9557–9569. <https://doi.org/10.1523/JNEUROSCI.19-21-09557.1999>.

Rodríguez, F., B. Quintero, L. Amores, D. Madrid, C. Salas-Peña, and C. Salas. 2021. “Spatial Cognition in Teleost Fish: Strategies and Mechanisms.” *Animals* 11: 2271. <https://doi.org/10.3390/ani11082271>.

Ryu, W. S., and A. D. T. Samuel. 2002. “Thermotaxis in *Caenorhabditis elegans* Analyzed by Measuring Responses to Defined Thermal Stimuli.” *Journal of Neuroscience* 22: 5727–5733. <https://doi.org/10.1523/JNEUROSCI.22-13-05727.2002>.

Tanimoto, Y., A. Yamazoe-Umemoto, K. Fujita, et al. 2017. “Calcium Dynamics Regulating the Timing of Decision-Making in *C. elegans*.” *eLife* 6: e21629. <https://doi.org/10.7554/eLife.21629>.

Tomioka, M., Y. Naito, H. Kuroyanagi, and Y. Iino. 2016. “Splicing Factors Control *C. elegans* Behavioural Learning in a Single Neuron by Producing DAF-2c Receptor.” *Nature Communications* 7: 11645. <https://doi.org/10.1038/ncomms11645>.

Wang, Y., X. Zhang, Q. Xin, et al. 2020. “Flexible Motor Sequence Generation During Stereotyped Escape Responses.” *eLife* 9: e56942. <https://doi.org/10.7554/eLife.56942>.

Yamazoe-Umemoto, A., K. Fujita, Y. Iino, Y. Iwasaki, and K. D. Kimura. 2015. “Modulation of Different Behavioral Components by Neuropeptide and Dopamine Signalings in Non-Associative Odor Learning of *Caenorhabditis elegans*.” *Neuroscience Research* 99: 22–33. <https://doi.org/10.1016/j.neures.2015.05.009>.

Zhao, B., P. Khare, L. Feldman, and J. A. Dent. 2003. “Reversal Frequency in *Caenorhabditis elegans* Represents an Integrated Response to the State of the Animal and Its Environment.” *Journal of Neuroscience: The Official Journal of the Society for Neuroscience* 23: 5319–5328. <https://doi.org/10.1523/JNEUROSCI.23-12-05319.2003>.

## Supporting Information

Additional supporting information can be found online in the Supporting Information section.